

An improved high-precision polyhedron SBFEM with combinatorial interpolation strategies

Xiupeng Nie^{a,b}, Degao Zou^{a,b}, Kai Chen^{a,b,*}, Guoyang Yi^{a,b}, Xianjing Kong^{a,b}

^a The State Key Laboratory of Coastal and Offshore Engineering, Dalian University of Technology, Dalian, Liaoning 116024, China

^b School of Hydraulic Engineering, Dalian University of Technology, Dalian, Liaoning 116024, China

ARTICLE INFO

Keywords:

SBFEM
Polyhedron
Mixed-order element
Octree algorithms
Bending deformation
Stress concentration

ABSTRACT

Computational accuracy and solution efficiency are crucial indicators for evaluating the performance of finite element numerical algorithms, and the corresponding improvements in these areas are the motivation for the development of computational science. In this paper, a flexible and high-precision polyhedron algorithm is proposed in conjunction with SBFEM and the triangle/quadrilateral interpolation functions. The main content can be summarized as follows: The construction equations for a mixed-order polyhedron element are derived, meanwhile, a generalized procedural framework is designed for multi-performance applications, including automatic elements type identification, coupled solutions, and dynamic storage, and the integrated development is completed based on self-developed software GEODYNA. The correctness, convergence and practicability of the proposed method are demonstrated through several examples in different dimensions. The results show that the proposed method obtains results with an error of <3 % compared to theoretical solutions and the fine numerical solutions, while significantly reducing computational costs; Besides, the proposed method overcomes the limitations of conventional methods on mesh shape and can be seamlessly integrated with octree algorithms, which offers a powerful technical means for the efficient and high-precision analyses of bending deformation and stress concentration problems. It is foreseeable that a good application potential in high-precision structural analysis would be revealed.

1. Introduction

In recent years, numerical simulation methods have gained widespread application in both theoretical and engineering analyses due to their operational simplicity and practical effectiveness. Among these methods, the finite element method (FEM) stands out as one of the most prevalent numerical techniques. Owing to its mesh discretization capabilities, FEM enables the straightforward and efficient handling of complex geometrical models under different conditions. As a result, FEM has been extensively utilized in various fields, including geotechnical engineering [1,2], medical sciences [3,4], and aerospace applications [5,6], etc.

The results obtained from FEM are influenced by the quality of the discretized meshes. In three-dimensional(3D) problems, the types of elements available in FEM libraries mainly include tetrahedron and hexahedron elements. Tetrahedron elements have good adaptability to complex geometries, but they exhibit somewhat poorer accuracy relative to the hexahedron elements [7,8], and the higher-order form is

required to achieve satisfactory computational results, which will lead to a greater computational effort. Hexahedron elements are generally recognized for their computational efficiency and stability [9]; however, they may be less suited to the geometric adaptability demands of complex models. Beyond hexahedron elements, irregular polyhedron elements with an arbitrary number of faces appear to be a viable alternative [10].

Polyhedron elements offer the capability to maintain the geometric properties of 3D models with higher fidelity, thus providing a distinct advantage in terms of geometric adaptability. Presently, various mesh discretization techniques are available for generating polyhedral elements [11–13], among which the octree-based method is more widely adopted. In a 3D problem domain, the octree technique facilitates the discretization of the model into polyhedron, tetrahedron and hexahedron elements. During this process, hanging nodes tend to emerge at the interfaces where elements of differing sizes meet. Nevertheless, the direct calculations for polyhedron and tetrahedron/hexahedron elements with hanging nodes in traditional FEM will be awkward and

* Corresponding author.

E-mail address: chenkai@dlut.edu.cn (K. Chen).

<https://doi.org/10.1016/j.enganabound.2024.105991>

Received 11 July 2024; Received in revised form 3 October 2024; Accepted 4 October 2024

Available online 8 October 2024

0955-7997/© 2024 Elsevier Ltd. All rights are reserved, including those for text and data mining, AI training, and similar technologies.

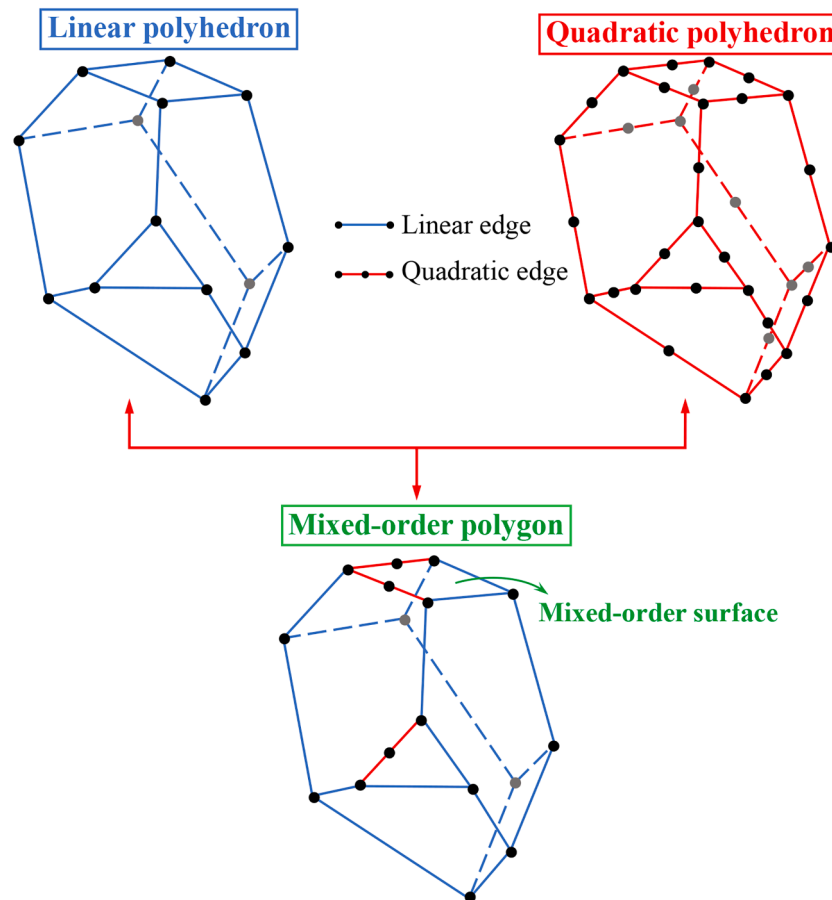


Fig. 1. Illustration of the mixed-order polyhedron element.

laborious. In order to avoid difficulties in coping with generated meshes for 3D complex models, some effective numerical methods have been developed.

The scaled boundary finite element method (SBFEM) proposed by Song and Wolf [14,15] is naturally conducive to the solution of complex 3D computational meshes. As a semi-analytical numerical technique, SBFEM utilizes the finite element concept to discretize only the boundaries of the subdomains, which makes the solutions numerical in the circumferential direction while analytical in the radial direction [16, 17]. This distinctive characteristic allows SBFEM to effectively calculate polyhedron elements with any number of multi-node faces. After continuous research and development by Song [18–20], researchers have recently conducted related studies on SBFEM and achieved some fruitful results. Du et al. [21–23] applied SBFEM to simulate the crack propagation problems, and this method provides a new approach to modeling fracture problems and has proved to be promising. Ooi et al. [24,25] proposed an adaptive refinement strategy using SBFEM based on the quadtree technique, the results show that the proposed method is an effective means for improving computational efficiency compared to uniform refinement. Liu et al. [26,27] extended 3D SBFEM to model acoustic problems in the time domain, and the excellent practicality of the proposed method in modeling acoustic problems with complex geometry has been demonstrated. Zhang et al. [28,29] developed novel explicit solvers utilizing the characteristics of octree meshes, showing high performance in terms of execution conditions and computational speed. Zhao et al. [30–34] established a scaled boundary perfectly matched layer to research the wave problems in a 3D unbounded domain, and the proposed method has proven reliable for engineering problems. Liu et al. [35,36] developed the buckling analysis of the functionally graded material sandwich plates based on 3D SBFEM. In

addition, SBFEM has seen considerable advancements through the efforts of researchers in recent years and has been applied in various fields, such as nonlinear analysis [37–40], Cosserat continuum analysis [41], automatic image-based topology optimization [42], direct point-cloud numerical analysis [43], and the stress analysis [44], etc.

It is well established that higher-order elements offer greater computational accuracy at the same mesh density levels, and they are especially beneficial for problems involving bending effects or large stress gradient changes. Noteworthy, so far, the majority of research on the SBFEM has primarily focused on linear elements, with little attention being given to higher-order elements for both 2D and 3D problems. In 3D scenarios, the boundary surface elements of the SBFEM are generally derived from 2D parent elements. In 2D quadrilateral parent elements, the typical linear interpolation functions are Lagrange-type functions [45,46], and the “Serendipity” elements are used for quadratic quadrilateral elements [47], ensuring that each edge possesses bending properties. For triangular elements, similar Lagrangian functions and their quadratic forms are also applicable [48]. With regard to polygon elements, a commonly used linear interpolation function is the mean-value coordinates [49], and a quadratic form derived from serendipity polygon elements has also been developed [50]. Up to now, the finite element researches involving the 2D higher-order elements have already made corresponding advancements [51,52].

As mentioned above, although higher-order elements possess inherent advantages, their computational cost and complexity will increase due to the high number of degrees of freedom (Dofs). Furthermore, in many application scenarios, linear elements are often adequate for computational requirements, whereas quadratic elements are required only in specific contexts. Therefore, the development of an element type that is compatible with both linear and quadratic forms

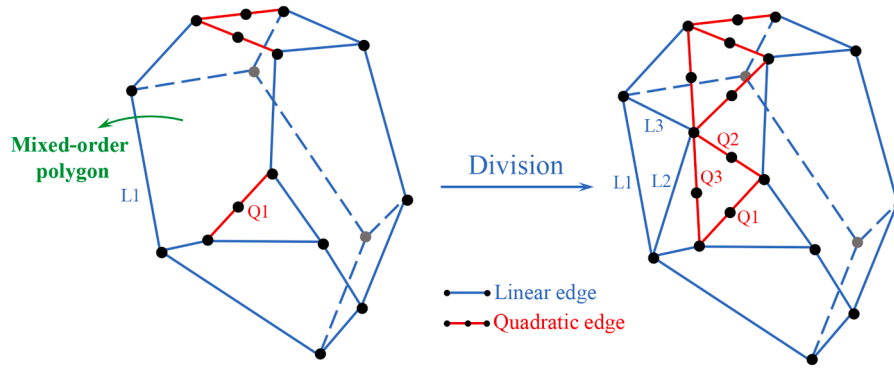


Fig. 2. The division process of the mixed-order polygon.

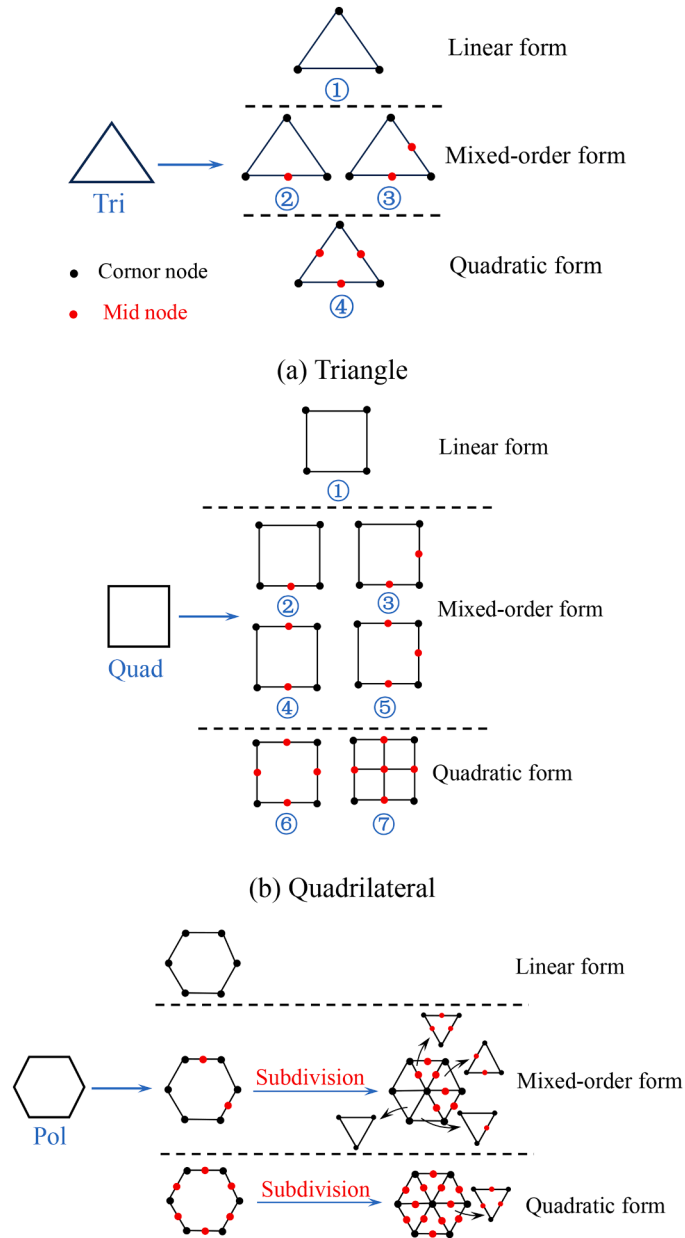


Fig. 3. Different surface element types.

appears to be a practical approach. In this vein, the new element forms called “mixed-order” elements, which enable the coexistence of linear and quadratic edges within the same element, have been developed for the 2D polygons [53] and 3D hexahedrons [54]. To achieve high-precision and efficient analysis of 3D complex geometries, it is essential to exploit an effective mixed-order polyhedron element that incorporates the features of these aforementioned element types.

In this paper, a mixed-order polyhedron element is developed within the SBFEM framework for 3D high-precision and high-efficiency analysis. The surfaces of the polyhedron with different orders are interpolated in the form of FEM. Besides, to decrease the computational efforts, triangular and quadrilateral surfaces with hanging nodes are flexibly interpolated and scaled by the serendipity element interpolation functions. Finally, the accuracy and practicality of the proposed method are validated and discussed through several examples.

The remainder of this paper is organized as follows. Section 2 provides a brief description of the mixed-order polyhedron elements. The theoretical formulation of the 3D SBFEM for the mixed-order polyhedron elements is presented in Section 3. In Section 4, several numerical examples are presented to demonstrate the accuracy, efficiency, and practicality of the proposed method in addressing different problems. Section 5 demonstrates the practicality of the method proposed for complex geometric structures. Finally, conclusions are stated in Section 6.

2. Summary of the mixed-order polyhedron element

2.1. Definition of the mixed-order polyhedron element

As detailed in Section 1, the incorporation of both linear and quadratic edges facilitates the construction of mixed-order polyhedron elements, and the corresponding explanatory diagram is provided in Fig. 1. The polyhedron comprises triangular, quadrilateral, and polygonal surface elements, with both its fully linear and fully quadratic forms initially provided. Depending on the specific requirements, each edge of the polyhedron element can be selectively allocated to either linear or quadratic order, which is the source of the term “mixed-order”. This mixed-order configuration integrates the advantages of both linear and quadratic forms, thereby enhancing flexibility and optimizing the initial mesh generation process.

2.2. Processing of the mixed-order polygon surface

With regard to the mixed-order polygon surfaces, although the corresponding serendipity interpolation function for polygonal finite elements has been derived, the total number of mixed-order types for polygons with n ($n > 4$) nodes is in the hundreds, which renders the method impractical for interpolating mixed-order polygon surfaces.

Here, we divided the mixed-order polygon surface elements into n sub-triangular elements, as shown in Fig. 2. If at least one edge of the

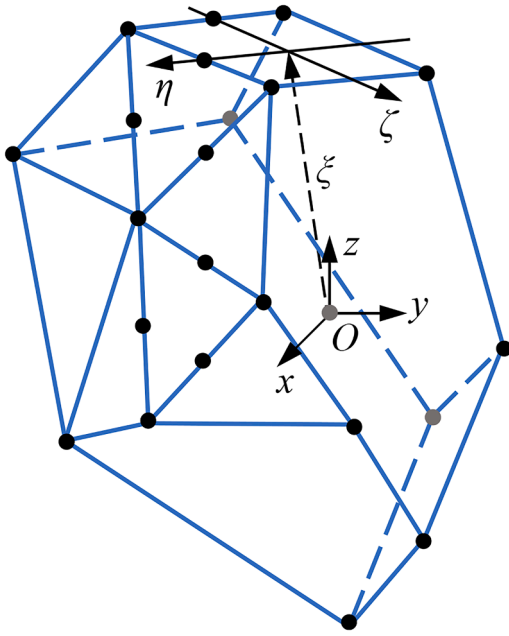
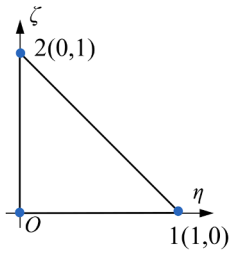
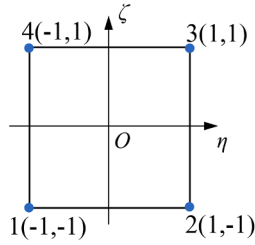


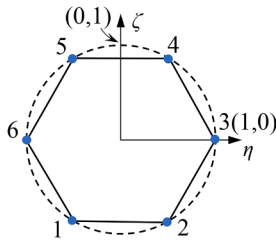
Fig. 4. The polyhedron element in two coordinate systems.



(a) Triangle element



(b) Quadrilateral element



(c) Polygon element

Fig. 5. Parent elements for different surface types.

polyhedron is in quadratic form, the subdivision process will be implemented. The remaining two edges, Q2 and Q3, of the newly generated sub-triangle, which corresponds to the quadratic edge Q1, will also be quadratic. In a similar manner, the edges L2-L3 of the new sub-triangle, which corresponds to the linear outer edge L1, are likewise linear. By this means, mixed-order polygons can be transformed into multiple mixed-order triangles, thus greatly reducing the processing difficulty.

2.3. Surface element types

The mixed-order triangles, quadrilaterals, and linear polygon surfaces are also presented in the polyhedron, as seen in Fig. 2.

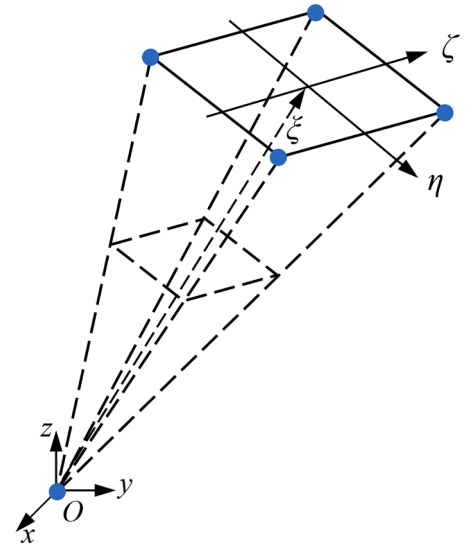


Fig. 6. The scaling diagram of the surface element.

Consequently, all surface element types within the polyhedron element are outlined in Fig. 3.

The number of types of order forms for triangles and quadrilaterals is 4 and 7, respectively. However, for polygon surface elements, the order types are not consistent. In particular, its linear mode is still represented as a polygon, while its mixed-order form, one of which is shown in Fig. 3 (c), comprises n triangle elements of varying orders. Lastly, the quadratic polygon elements are subdivided into n quadratic triangle elements. Therefore, the aforementioned elements encompass all surface element types for mixed-order polyhedron elements.

3. SBFEM for the mixed-order polyhedron element

3.1. Coordinates transformation

In the SBFEM theory, each polyhedron element in the Cartesian coordinates can be transformed into the scaled boundary coordinates. The polyhedron element with the scaled boundary coordinates (ξ, η, ζ) and the Cartesian coordinates (x, y, z) is shown in Fig. 4. A scaling center O is assumed to lie inside the element domain, which needs to satisfy being directly visible to the arbitrary node on the boundary of the element. In SBFEM, only the boundary of the polyhedron element needs to be discretized by means of the surface elements, and the surface elements can be represented under local boundary coordinates (η, ζ) , then the surface element is scaled by the radial coordinate ξ , as illustrated in Fig. 4.

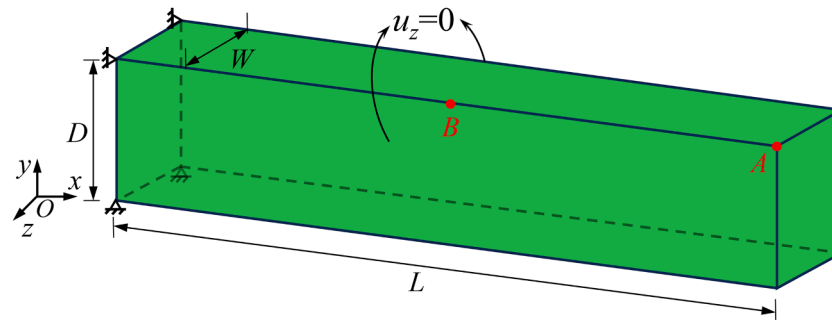
The parent element types of different surface elements in the polyhedron are shown in Fig. 5, and the scaling diagram of the surface element in SBFEM is illustrated in Fig. 6 through the quadrilateral surface element. In scaled boundary coordinates, any point in the polyhedron element can be described as:

$$\begin{aligned} x(\xi, \eta, \zeta) &= x_0 + \xi N(\eta, \zeta) \\ y(\xi, \eta, \zeta) &= y_0 + \xi N(\eta, \zeta) \\ z(\xi, \eta, \zeta) &= z_0 + \xi N(\eta, \zeta) \end{aligned} \quad (3.1)$$

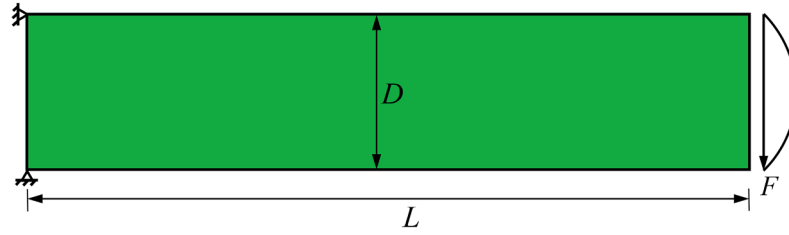
where (x_0, y_0, z_0) is the coordinate of the scaled center O in the Cartesian coordinate system, $N(\eta, \zeta)$ is the shape function of the surface element in the local coordinate system (η, ζ) .

3.2. SBFEM theory formulation

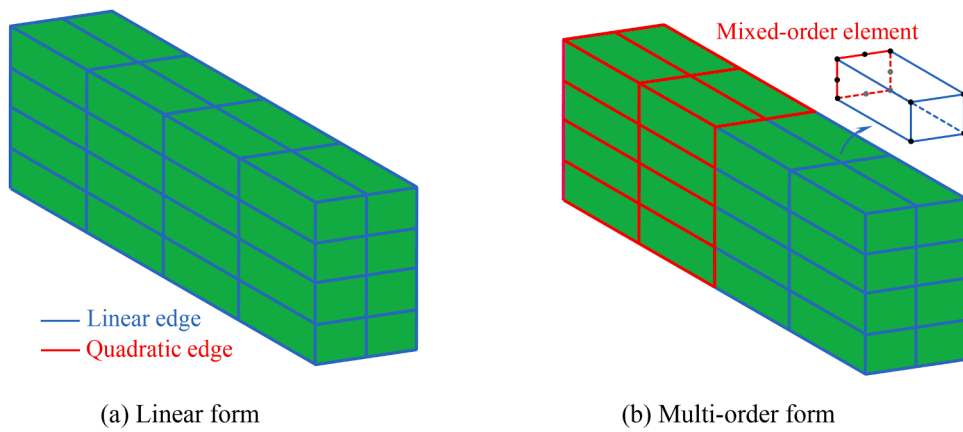
For SBFEM displacement $u(\xi, \eta, \zeta)$, an unknown radial displacement $u(\xi)$ along the radial lines is first introduced, and the displacement formulation is thus expressed as:



(a) Geometry and boundary conditions

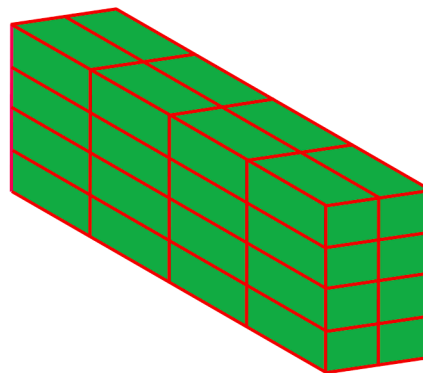


(b) Loading conditions

Fig. 7. Cantilever beam model for 2D plane stress problem.

(a) Linear form

(b) Multi-order form



(c) Quadratic form

Fig. 8. The 3D mesh of the cantilever beam model.

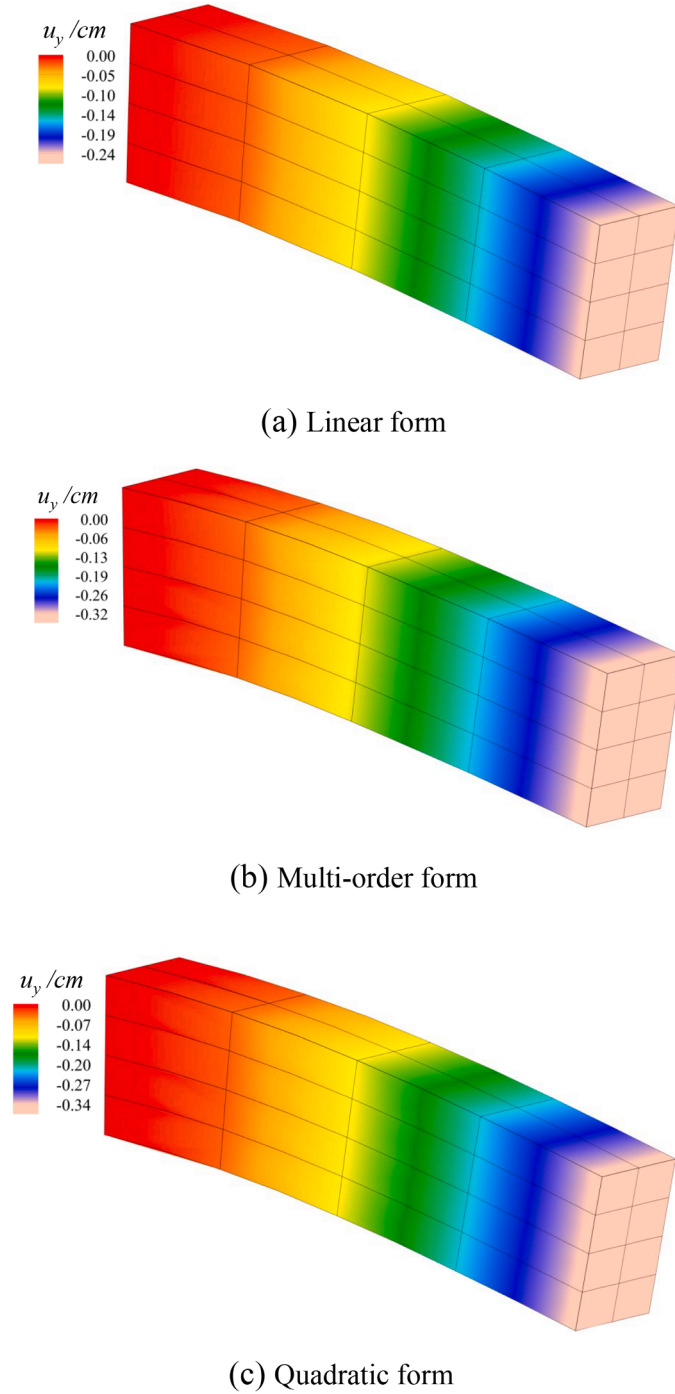


Fig. 9. Deformation modes (magnification $\times 20$) for the different mesh order forms.

Table 1
Comparison of u_y of observation points.

Mesh type	Point A		Point B		Dofs
	u_y/mm	Error/%	u_y/mm	Error/%	
Linear form	-2.442	31.33	-0.790	33.16	225
Multi-order form (The proposed method)	-3.435	3.40	-1.142	3.38	513
Quadratic form	-3.511	1.27	-1.173	0.76	735
Analytical solutions	-3.556	–	-1.182	–	–

$$u(\xi, \eta, \zeta) = \mathbf{N}_u(\eta, \zeta) \mathbf{u}(\xi) \quad (3.2)$$

where the shape functions $\mathbf{N}_u(\eta, \zeta)$ is expressed as $[N_1(\eta, \zeta), N_2(\eta, \zeta), \dots]$, \mathbf{I} is the 3×3 identity matrix.

Under the scaled boundary framework, the linear differential operator \mathbf{L} in 3D [14] is expressed as:

$$\mathbf{L} = \mathbf{b}_1 \frac{\partial}{\partial \xi} + \frac{1}{\xi} \left(\mathbf{b}_2 \frac{\partial}{\partial \eta} + \mathbf{b}_3 \frac{\partial}{\partial \zeta} \right) \quad (3.3)$$

where $\mathbf{b}_1(\eta, \zeta)$, $\mathbf{b}_2(\eta, \zeta)$ and $\mathbf{b}_3(\eta, \zeta)$ matrixes are defined as:

$$\mathbf{b}_1(\eta, \zeta) = \frac{1}{|\mathbf{J}|} \begin{bmatrix} y_{,\eta} z_{,\zeta} - z_{,\eta} y_{,\zeta} & 0 & 0 \\ 0 & z_{,\eta} x_{,\zeta} - x_{,\eta} z_{,\zeta} & 0 \\ 0 & 0 & x_{,\eta} y_{,\zeta} - y_{,\eta} x_{,\zeta} \\ 0 & x_{,\eta} y_{,\zeta} - y_{,\eta} x_{,\zeta} & z_{,\eta} x_{,\zeta} - x_{,\eta} z_{,\zeta} \\ x_{,\eta} y_{,\zeta} - y_{,\eta} x_{,\zeta} & 0 & y_{,\eta} z_{,\zeta} - z_{,\eta} y_{,\zeta} \\ z_{,\eta} x_{,\zeta} - x_{,\eta} z_{,\zeta} & y_{,\eta} z_{,\zeta} - z_{,\eta} y_{,\zeta} & 0 \end{bmatrix} \quad (3.4)$$

$$\mathbf{b}_2(\eta, \zeta) = \frac{1}{|\mathbf{J}|} \begin{bmatrix} zy_{,\zeta} - yz_{,\zeta} & 0 & 0 \\ 0 & xz_{,\zeta} - zx_{,\zeta} & 0 \\ 0 & 0 & yx_{,\zeta} - xy_{,\zeta} \\ 0 & yx_{,\zeta} - xy_{,\zeta} & xz_{,\zeta} - zx_{,\zeta} \\ yx_{,\zeta} - xy_{,\zeta} & 0 & zy_{,\zeta} - yz_{,\zeta} \\ xz_{,\zeta} - zx_{,\zeta} & zy_{,\zeta} - yz_{,\zeta} & 0 \end{bmatrix} \quad (3.5)$$

$$\mathbf{b}_3(\eta, \zeta) = \frac{1}{|\mathbf{J}|} \begin{bmatrix} yz_{,\eta} - zy_{,\eta} & 0 & 0 \\ 0 & zx_{,\eta} - xz_{,\eta} & 0 \\ 0 & 0 & xy_{,\eta} - yx_{,\eta} \\ 0 & xy_{,\eta} - yx_{,\eta} & zx_{,\eta} - xz_{,\eta} \\ xy_{,\eta} - yx_{,\eta} & 0 & yz_{,\eta} - zy_{,\eta} \\ zx_{,\eta} - xz_{,\eta} & yz_{,\eta} - zy_{,\eta} & 0 \end{bmatrix} \quad (3.6)$$

Therefore, the strain field can be expressed as:

$$\varepsilon = \mathbf{L} \mathbf{u}(\xi, \eta, \zeta) = \mathbf{B}_1 \mathbf{u}(\xi)_{,\xi} + \frac{1}{\xi} \mathbf{B}_2 \mathbf{u}(\xi) \quad (3.7)$$

with

$$\begin{aligned} \mathbf{B}_1 &= \mathbf{b}_1 \mathbf{N}_u(\eta, \zeta) \\ \mathbf{B}_2 &= \mathbf{b}_2 \mathbf{N}_u(\eta, \zeta)_{,\eta} + \mathbf{b}_3 \mathbf{N}(\eta, \zeta)_{,\zeta} \end{aligned} \quad (3.8)$$

The stress field in the scaled boundary system is thus presented as:

$$\sigma = \mathbf{D} \left(\mathbf{B}_1 \mathbf{u}(\xi)_{,\xi} + \frac{1}{\xi} \mathbf{B}_2 \mathbf{u}(\xi) \right) \quad (3.9)$$

where \mathbf{D} is the plasticity matrix.

The 3D scaled boundary finite element equation in terms of the displacement is derived by the virtual work principle [55], which is written as:

$$\mathbf{E}_0 \xi^2 \mathbf{u}(\xi)_{,\xi\xi} + (2\mathbf{E}_0 + \mathbf{E}_1^T - \mathbf{E}_1) \xi \mathbf{u}(\xi)_{,\xi} + (\mathbf{E}_1^T - \mathbf{E}_2) \mathbf{u}(\xi) = 0 \quad (3.10)$$

in which \mathbf{E}_0 , \mathbf{E}_1 , and \mathbf{E}_2 are the coefficient matrices of the surface elements, and they are expressed as:

$$\begin{aligned} \mathbf{E}_0 &= \int_{-1}^1 \int_{-1}^1 \mathbf{B}_1^T \mathbf{D} \mathbf{B}_1 |\mathbf{J}| d\eta d\zeta \\ \mathbf{E}_1 &= \int_{-1}^1 \int_{-1}^1 \mathbf{B}_2^T \mathbf{D} \mathbf{B}_1 |\mathbf{J}| d\eta d\zeta \\ \mathbf{E}_2 &= \int_{-1}^1 \int_{-1}^1 \mathbf{B}_2^T \mathbf{D} \mathbf{B}_2 |\mathbf{J}| d\eta d\zeta \end{aligned} \quad (3.11)$$

3.3. Solution of SBFEM formulation

The solution procedure for Eq. (3.10) involving an order transformation can be derived from an intermediate variable $\mathbf{X}(\xi)$, and the obtained first-order homogeneous differential equation is shown in Eq. (3.13).

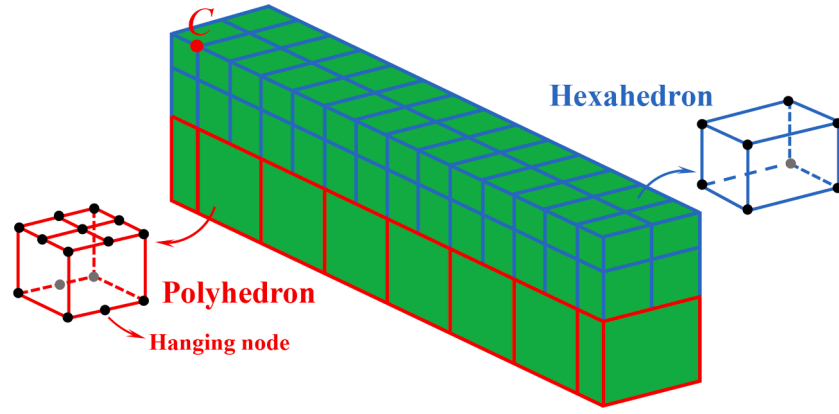


Fig. 10. The octree mesh of the cantilever beam model.

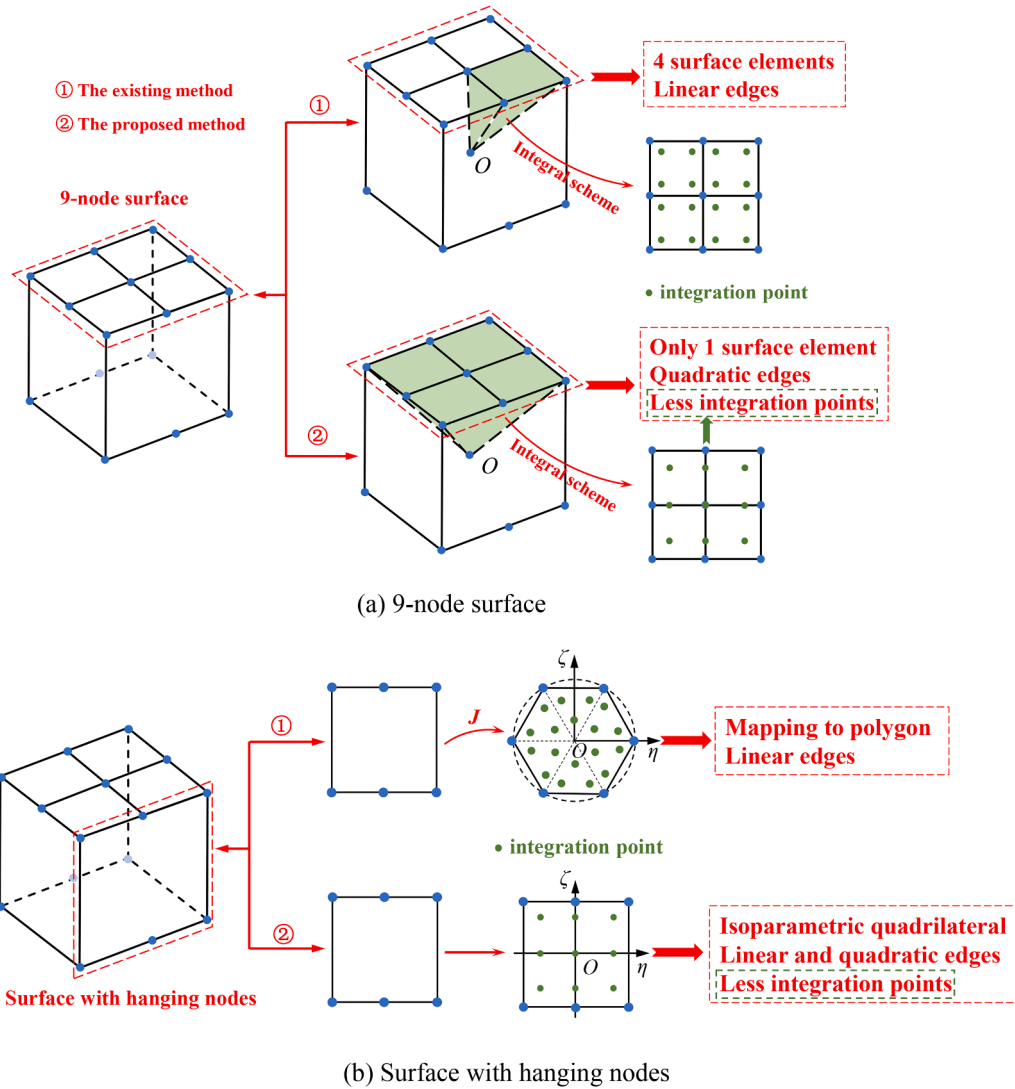


Fig. 11. Comparison of different methods for processing octree mesh.

$$\mathbf{X}(\xi) = \begin{bmatrix} \xi^{0.5} \mathbf{u}(\xi) \\ \xi^{-0.5} \mathbf{q}(\xi) \end{bmatrix} \quad (3.12)$$

$$\xi \mathbf{X}(\xi)_{,\xi} = -\mathbf{Z} \mathbf{X}(\xi) \quad (3.13)$$

where $\mathbf{q}(\xi)$ in Eq. (3.12) is the internal nodal forces, the Hamilton matrix

\mathbf{Z} is expressed as:

$$\mathbf{Z} = \begin{bmatrix} \mathbf{E}_0^{-1} \mathbf{E}_1^T - 0.5\mathbf{I} & -\mathbf{E}_0^{-1} \\ -\mathbf{E}_2 + \mathbf{E}_1 \mathbf{E}_0^{-1} \mathbf{E}_1^T & -(\mathbf{E}_1 \mathbf{E}_0^{-1} - 0.5\mathbf{I}) \end{bmatrix} \quad (3.14)$$

Eigenvalue decomposition towards the matrix \mathbf{Z} is executed to obtain

Table 2
Comparison of u_y for different methods.

Methods	Point A		Point B		Point C	
	u_y/mm	Error/%	u_y/mm	Error/%	u_y/cm	Error/%
The existing method	-3.219	9.40	-1.036	11.98	-0.043	58.25
The proposed method	-3.548	0.14	-1.141	3.06	-0.099	3.88
Analytical solutions	-3.553	-	-1.177	-	-0.103	-

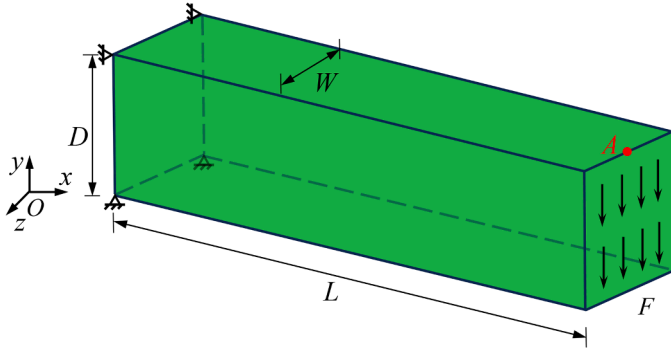
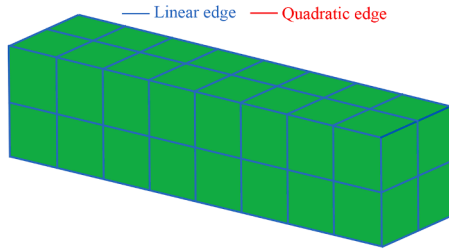
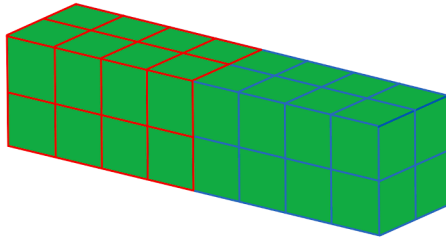


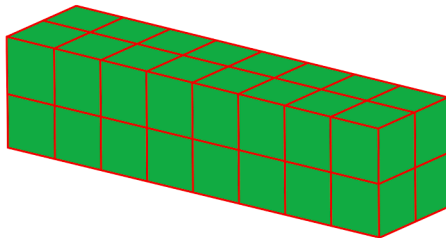
Fig. 12. Comparison of different methods for processing octree mesh.



(a) Linear form

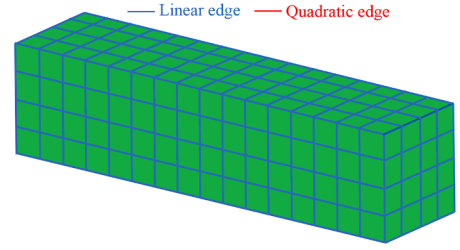


(b) Multi-order form

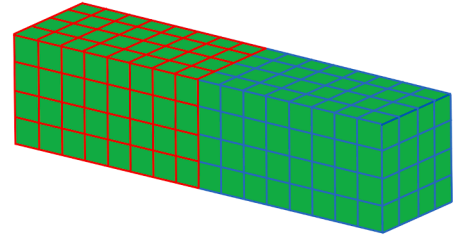


(c) Quadratic form

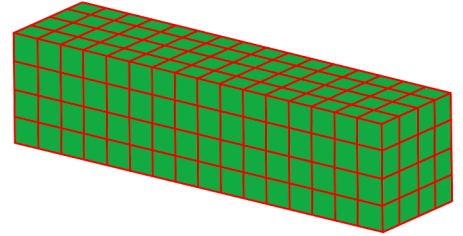
Fig. 13. $8 \times 2 \times 2$ Mesh of the 3D cantilever beam model.



(a) Linear form



(b) Multi-order form



(c) Quadratic form

Fig. 14. $16 \times 4 \times 4$ Mesh of the 3D cantilever beam model.

$$\mathbf{Z} \begin{bmatrix} \psi_u \\ \psi_q \end{bmatrix} = \begin{bmatrix} \psi_u \\ \psi_q \end{bmatrix} \mathbf{S}_n \quad (3.15)$$

In Eq. (3.15), \mathbf{S}_n is a diagonal matrix consisting of the real parts of the eigenvalues of the \mathbf{Z} . ψ_u and ψ_q are the eigenvector matrix. In a bounded domain, the general solutions of Eq. (3.13) are solved as:

$$\begin{aligned} \mathbf{u}(\xi) &= \psi_u \xi^{-(S_n+0.5I)} \mathbf{c} \\ \mathbf{q}(\xi) &= \psi_q \xi^{-(S_n-0.5I)} \mathbf{c} \end{aligned} \quad (3.16)$$

The integration constant matrix \mathbf{c} can be expressed by the node displacement \mathbf{u}_b on the element boundary:

$$\mathbf{c} = \psi_u^{-1} \mathbf{u}_b \quad (3.17)$$

The displacement field $u(\xi, \eta, \zeta)$ of the polyhedron element in the scaled boundary coordinates is then expressed as follows:

$$u(\xi, \eta, \zeta) = \mathbf{N}_u(\eta, \zeta) \psi_u \xi^{-(S_n+0.5I)} \psi_u^{-1} \mathbf{u}_b \quad (3.18)$$

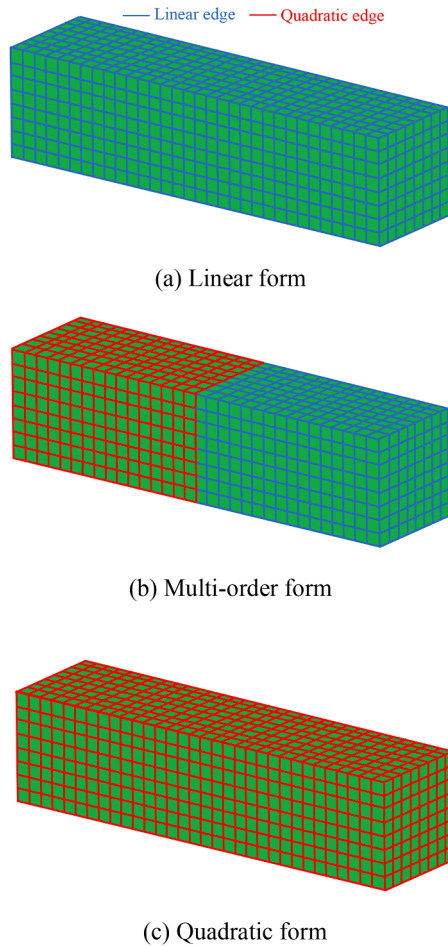
As with FEM, the shape functions $\Phi(\xi, \eta, \zeta)$ can be extracted as:

$$\Phi(\xi, \eta, \zeta) = \mathbf{N}_u(\eta, \zeta) \psi_u \xi^{-(S_n+0.5I)} \psi_u^{-1} \quad (3.19)$$

Further, the strain field can be represented as:

$$\varepsilon(\xi, \eta, \zeta) = [\mathbf{B}_1 \psi_u (-S_n - 0.5) + \mathbf{B}_2 \psi_u] \cdot \xi^{-(S_n+1.5I)} \psi_u^{-1} \mathbf{u}_b \quad (3.20)$$

$$\mathbf{B}_u = [\mathbf{B}_1 \psi_u (-S_n - 0.5) + \mathbf{B}_2 \psi_u] \cdot \xi^{-(S_n+1.5I)} \psi_u^{-1} \quad (3.21)$$

Fig. 15. $32 \times 8 \times 8$ Mesh of the 3D cantilever beam model.

4. Numerical examples

4.1. Cantilever beam of 2D plane stress problem

To evaluate the accuracy and efficiency of the proposed method, a numerical simulation for a classical cantilever beam of 2D plane stress problem is carried out, and the details of the example are described below.

4.1.1. Geometry and material parameters

A cantilever beam subject to a parabolic loading at the end is shown in Fig. 7. The length of the beam is $L = 480$ mm, the height is $D = 120$ mm, and the width is $W = 80$ mm. The boundary conditions of the model are also depicted in Fig. 7. The material of the beam is assumed to elasticity with Young's modulus $E = 30,000$ Pa, and Poisson's ratio $\nu = 0.25$. At the end face of the beam, a shear load with a parabolic distribution is applied. The total value of shear force is $F = 320$ N.

4.1.2. Mesh discretization

The first discretized 3D mesh of the cantilever beam is shown in Fig. 8(a), the selected mesh type is the linear hexahedron element, resulting in a total of 32 elements with 75 nodes. Secondly, a non-matched node mesh called "multi-order mesh" with linear, quadratic, and multi-order elements is discretized, as illustrated in Fig. 8(b). In this representation, the red lines depict the quadratic edges in the hexahedron element, while the blue lines represent the linear edges. Finally, a quadratic mesh shown in Fig. 8(c) is utilized for comparison purposes.

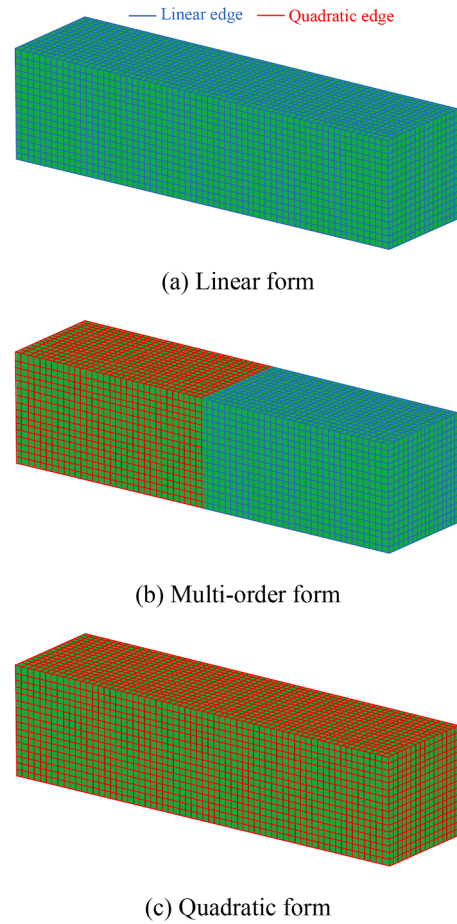
Fig. 16. $64 \times 16 \times 16$ Mesh of the 3D cantilever beam model.

Table 3

u_y Of point A for different mesh levels with different forms.

Mesh	u_y/m		
	Linear form	Multi-order form	Quadratic form
$8 \times 2 \times 2$	-0.231	-0.321	-0.324
$16 \times 4 \times 4$	-0.284	-0.345	-0.348
$32 \times 8 \times 8$	-0.327	-0.366	-0.369
$64 \times 16 \times 16$	-0.366	-0.379	-0.380 (Benchmark)

4.1.3. Accuracy verification

The computer software GEODYNA 8.0 [56], which integrates all aforementioned element classes in the meshes in Fig. 8, is applied to carry out the SBFEM calculations for the above meshes sequentially. Here, the y-direction displacements u_y of two observation points A and B, which have been marked in Fig. 7, are chosen as the comparison items for this example. The deformation modes for different mesh order forms are depicted in Fig. 9, and the corresponding calculated displacements are listed in Table 1. Besides, the analytical solutions of different points in this cantilever beam, which can be computed by Eq. (4.1) referenced from [57], are also included in Table 1.

$$u_y = \frac{F}{6EI} \left[3\nu y^2(L-x) + (4+5\nu) \frac{D^2 x}{4} + (3L-x)x^2 \right] \quad (4.1)$$

where I is the moment of inertia of the cross-section of the cantilever beam.

As illustrated in Table 1, numerical calculations performed with a linear mesh show significant discrepancies when compared to theoretical solutions, largely due to the shear-locking behavior of linear

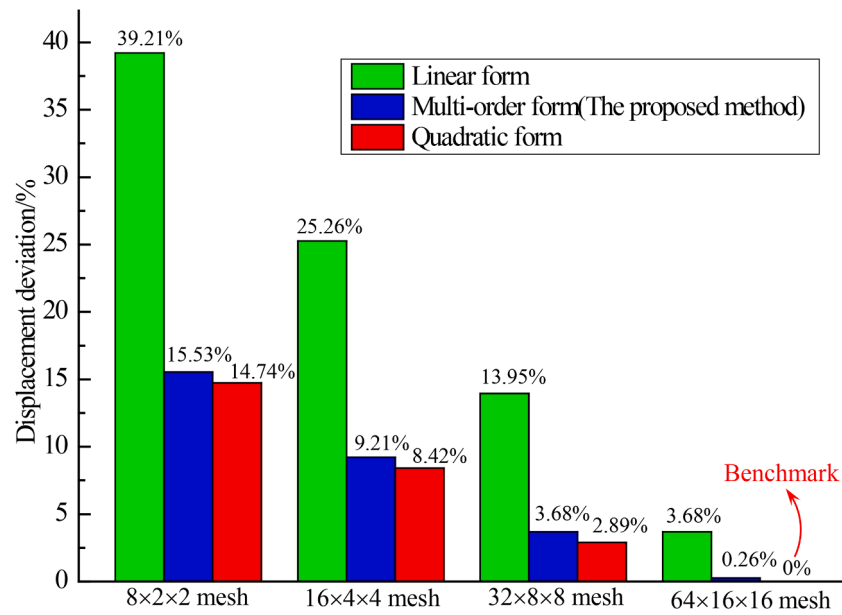


Fig. 17. Comparison of A-point displacement derivations for different mesh levels.

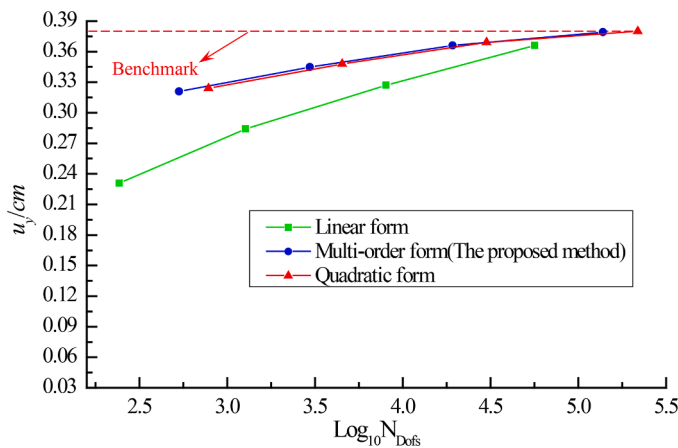


Fig. 18. Comparison of A-point displacement derivations for different mesh levels.

elements under bending loads. Conversely, although a quadratic mesh demonstrates substantially improved bending performance, there is a notable increase in computational workload, as evidenced by a significant rise in Dofs. In contrast, the multi-order mesh computed using the proposed method exhibits excellent results with an error of $< 4\%$. Importantly, the computational cost is notably reduced compared to the quadratic mesh. Therefore, the proposed method demonstrates reliable accuracy.

4.1.4. Calculation of octree mesh

Another advantage of the proposed method presented in this paper lies in its capacity to directly compute and process hanging nodes within the octree mesh, thus offering a novel approach to the octree mesh calculations. To demonstrate this advantage, the cantilever beam in this example is instead discretized using the octree technique. The resulting octree mesh, depicted in Fig. 10, consists of a total of 64 elements and 162 nodes. Specifically, the finer elements at the upper levels are all hexahedron, while the larger elements with hanging nodes at the lower levels are polyhedron.

The comparison of different methods for processing octree mesh is illustrated in Fig. 11. While the processing approach of the proposed

method for octree mesh is simplified, its improvement in computational performance remains unknown. Hence, calculations for different methods are conducted in this section, and the results are tabulated in Table 2. Notably, an observation point C near the end of the cantilever shown in Fig. 10, where the maximum bending moment in the existing mesh is located, is added for presentation of the calculation results.

As shown in Table 2, compared to the existing methods, the proposed method gives numerical results that can be closer to the analytical solutions. This improvement primarily stems from the treatment of edges with hanging nodes in the octree mesh as quadratic forms, which are therefore endowed with bending properties, resulting in computationally superior values under shear loading.

4.2. 3D cantilever beam

4.2.1. Geometry and material parameters

In this example, a 3D cantilever beam subjected to a uniform end-shear force is modeled (Fig. 12), the geometry of this model is also depicted in Fig. 12. The length of the beam is $L = 5$ m, the width is $W = 1$ m, and the height is $D = 1$ m. The material is assumed to be homogeneous with Young's modulus $E = 1$ GPa, Poisson's ratio $\nu = 0.3$. The beam is fixed on the left end plane by constraining the displacement $u_x = u_y = u_z = 0$ as the boundary condition. The right end plane of the cantilever beam is subjected to a uniform shear force $F = 1 \times 10^6$ N in the y-direction.

4.2.2. Mesh discretization

To better discuss the convergence and accuracy of the proposed method, four levels of mesh refinement are adopted in this model, as shown in Figs. 13-16, in which the number of discretized hexahedron elements in the dimensions of length, width, and height is $8 \times 2 \times 2$, $16 \times 4 \times 4$, $32 \times 2 \times 2$, and $64 \times 16 \times 16$ respectively. Each mesh level contains linear, multi-order, and quadratic forms, and similarly, the elements on the left half of the model are selected as quadratic elements in the multi-order mesh.

4.2.3. Calculation results

Numerical simulation calculations are conducted for different mesh levels with different forms. For this example, the focus is on observing the y-direction displacements u_y of point A, as illustrated in Fig. 12. The results are summarized in Table 3, where the values obtained from the

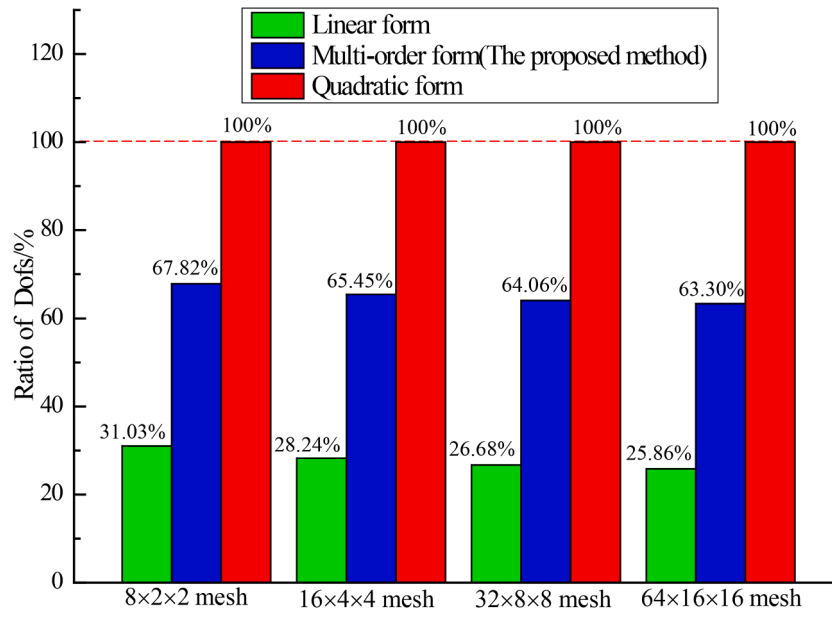


Fig. 19. The Dofs ratio of different order forms to quadratic forms for each mesh level.

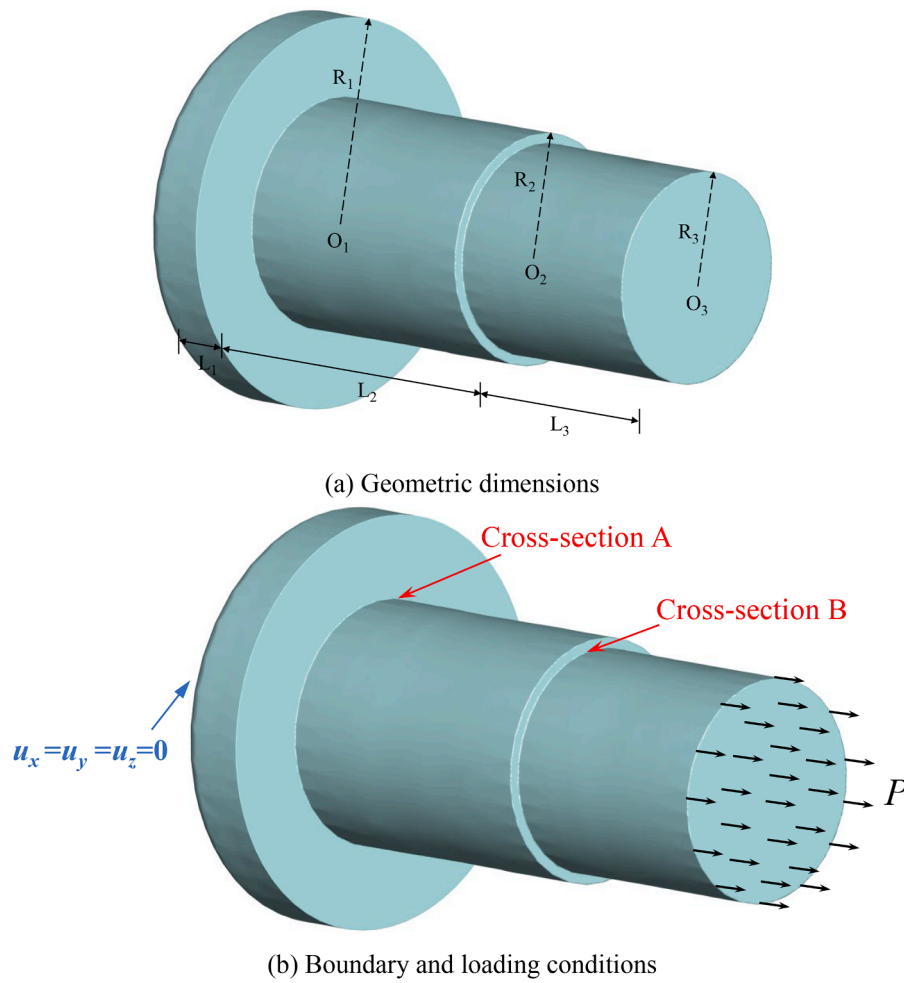
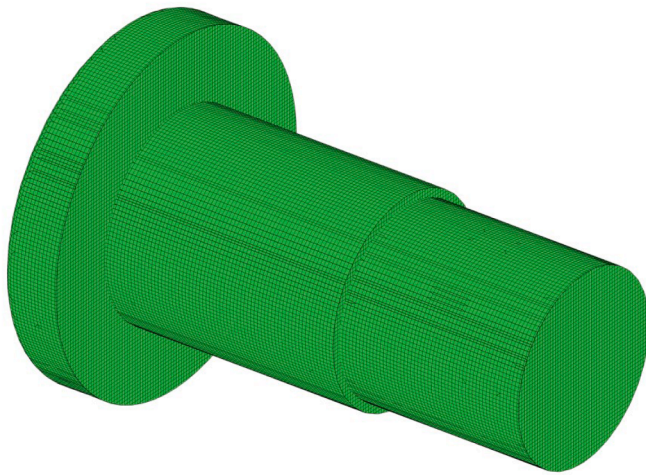
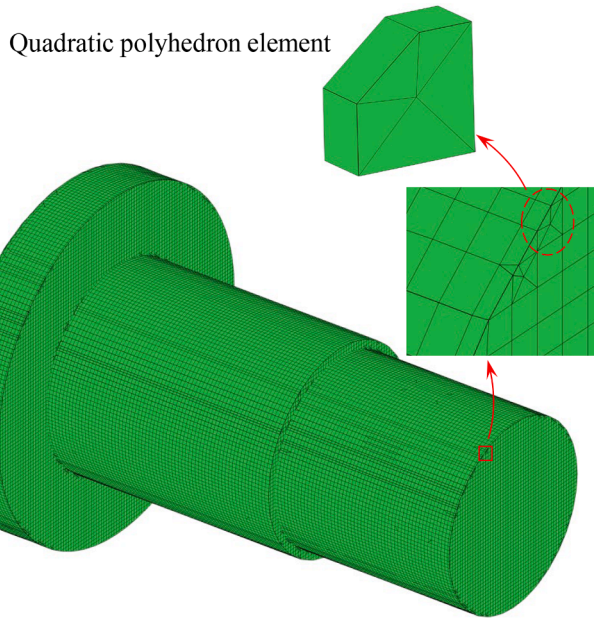


Fig. 20. Detailed information of the machine screw.



(a) Linear mesh



(b) Quadratic mesh

Fig. 21. Global refined mesh of the machine screw.

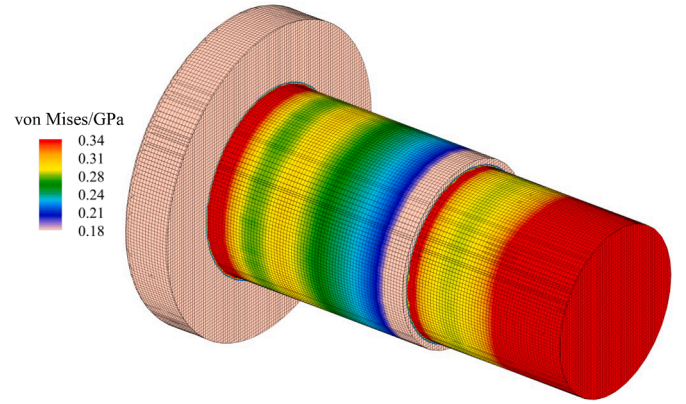
Table 4

The details of different method schemes.

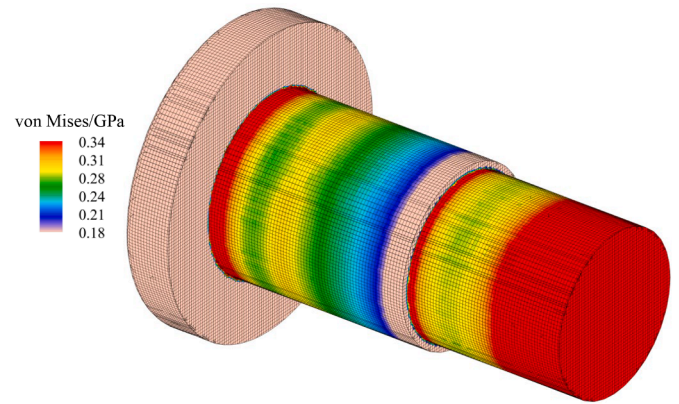
Element types	Element numbers	Percent/%
Tetrahedron	376	0.10
Hexahedron	354,478	95.91
Polyhedron	14,749	3.99

most refined quadratic mesh (specifically, the $64 \times 16 \times 16$ mesh) serve as the benchmark for comparison.

To facilitate visualization, the calculated results presented in Table 3 are expressed as deviations from the established benchmark, as illustrated in the column diagram in Fig. 17. For the same mesh refinement level, the quadratic form delivers the highest accuracy, followed closely by the multi-order form, which shows a minimal deviation of $<1\%$ from the quadratic form. Fig. 18 plots the displacements for different mesh



(a) Linear mesh



(b) Quadratic mesh

Fig. 22. von Mises stresses for global refined mesh in the machine screw.

orders against the number of Dofs, with positive displacement values plotted along the longitudinal axis for clarity. It is evident that across different mesh refinement levels, both the quadratic and multi-order forms demonstrate faster convergence rates.

The comparisons of Dofs for each mesh level with different forms are shown in Fig. 19. At the same mesh level, compared to the quadratic form, the linear form has the fewest Dofs but the computational accuracy cannot be guaranteed; In contrast, the multi-order form can ensure the solution accuracy with an approximately 35 % reduction in the number of Dofs compared to the quadratic form.

4.3. The machine screw

In order to demonstrate the effect of the proposed method in dealing with the stress concentration problem, a machine screw is analyzed in this section.

4.3.1. Geometry and material parameters

The machine screw shown in Fig. 20 consists of a screw cap and two cylindrical screw arbors with different sizes, the lengths of these components are $L_1=1.27$ cm, $L_2=5.33$ cm, and $L_3=5.47$ cm, respectively, the radius of the screw cap is $R_1=3.73$ cm and the radii of the two screw arbors are $R_2=2.21$ cm and $R_3=2.02$ cm respectively. All nodes at the cap end of the screw are constrained in displacement in the x , y , and z directions, and the right end face is subjected to a traction of $P = 0.2$ GPa. The material type of the screw is assumed to be stainless steel, which follows the elastic criterion with the parameters of Young's modulus $E = 200$ GPa, Poisson's ratio $\nu=0.3$, and the density $\rho=7.8$ g/

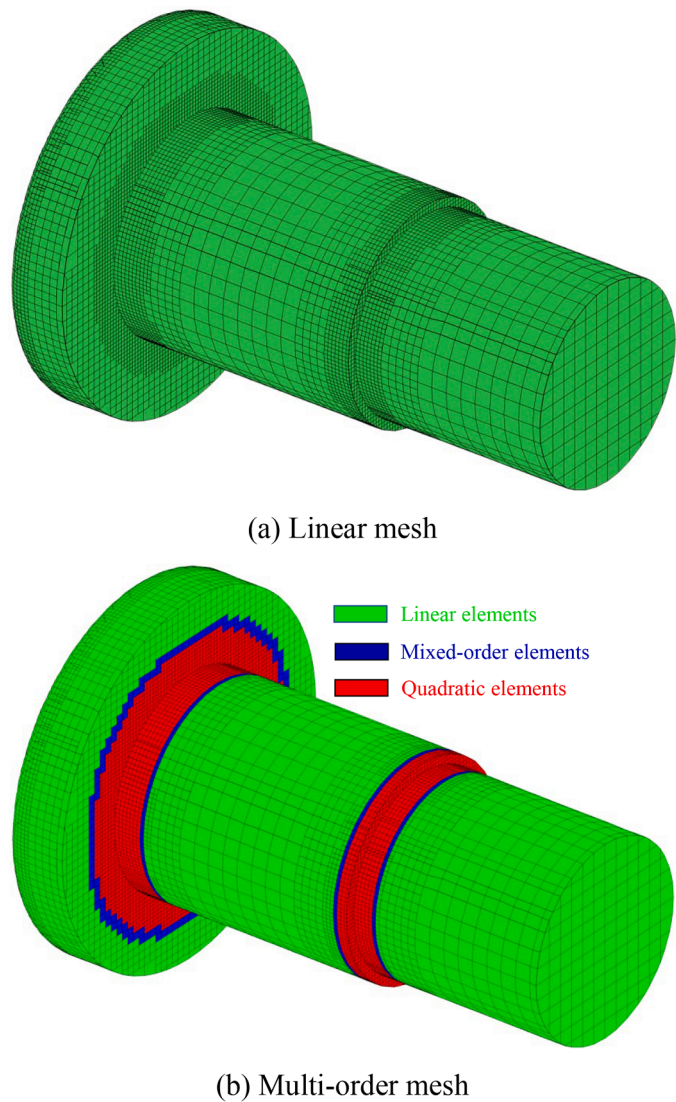


Fig. 23. Local refined mesh of the machine screw.

cm³.

4.3.2. Mesh discretization

For this 3D geometry, a global fined linear mesh with an element size of 0.08 cm is initially adopted for discretizing the computational domain, producing a total of 369,603 elements with 386,045 nodes, the generated mesh is shown in Fig. 21(a). Detailed information on the element composition is provided in Table 4. Subsequently, as depicted in Fig. 21(b), a global quadratic mesh is created by elevating the order of the linear mesh for conducting the respective analyses. In accordance with the methodology detailed in Section 2.2, the order elevation of polygonal surface elements proceeds is performed.

4.3.3. Calculation of the global refined mesh

Fig. 22 shows the stress analysis results for the von Mises stress of this machine screw. Obviously, the stress concentration phenomenon happens on the variable cross-sections between screw arbors of different sizes. Here, the two variable cross-sections are named Cross-sections ‘A’ and ‘B’, as shown in Fig. 20. The von Mises stress extreme values corresponding to the linear and quadratic meshes are 0.84 GPa and 0.85 GPa in cross-section A, and 0.49 GPa and 0.50 GPa in cross-section B. Analysis indicates that the extreme stress values derived from the two mesh orders exhibit a minimal discrepancy, implying that the

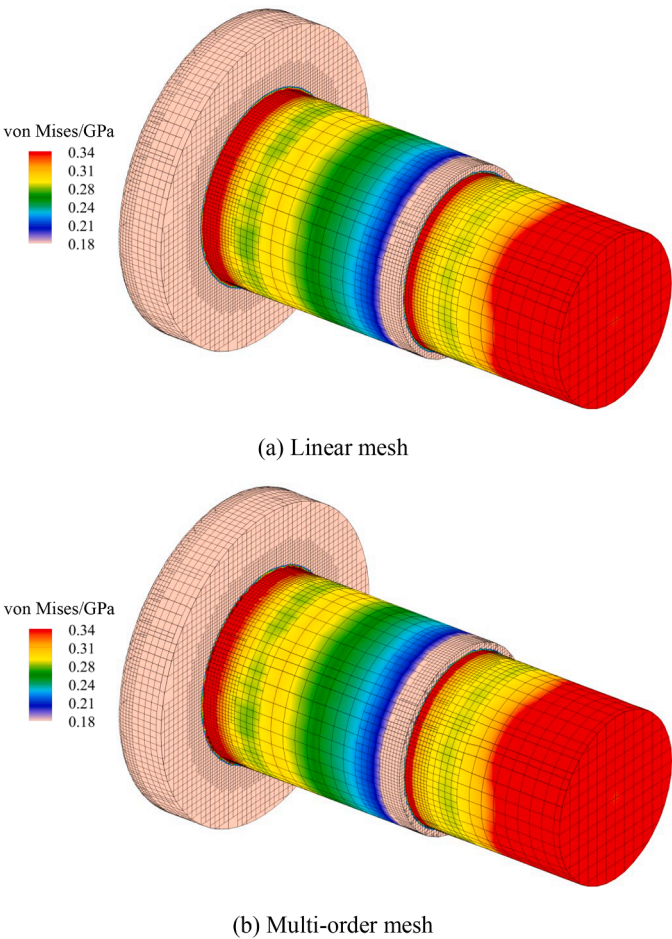


Fig. 24. von Mises stresses for local refined mesh in the machine screw.

Table 5
von Mises stress extreme values for different meshes.

Mesh type	Mesh form	Stress extreme values/GPa(Error/%)	
		Cross-section A	Cross-section B
Global refined mesh	Quadratic	0.85 (Benchmark)	0.50 (Benchmark)
	Linear	0.84 (1.19)	0.49 (2.00)
Local refined mesh	Multi-order (the proposed method)	0.83 (2.35)	0.48 (4.00)
	Linear	0.79 (7.06)	0.45 (10.00)

computational outcomes have achieved convergence at this mesh density. Thus, the stress results obtained from the quadratic mesh calculations are taken as benchmarks.

4.3.4. Calculation of the local refined mesh

Given the high computational costs associated with the globally refined mesh, the octree technique is employed in this section to achieve local refinement of the model. The discretized computational mesh is shown in Fig. 23(a), where elements sized at 0.08 cm are applied to the stress concentration regions identified in Fig. 21, while the remaining areas use elements sized at 0.5 cm. Consequently, a total of 42,238 elements and 93,063 nodes are generated. Furthermore, the elements within the stress concentration regions are upgraded to quadratic forms, resulting in a mesh with multi-order elements, as illustrated in Fig. 23 (b). It should be noted that the octree meshes in this model are processed by means of the proposed method, wherein the triangular and quadrilateral surfaces with hanging nodes are transformed according to the

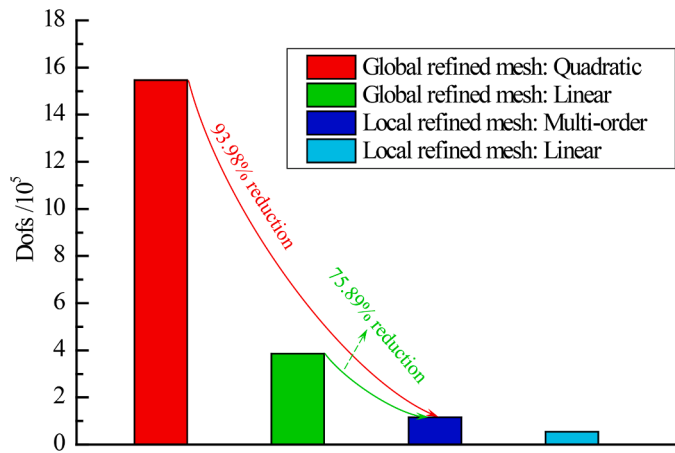


Fig. 25. The comparison of Dofs of different mesh order forms.

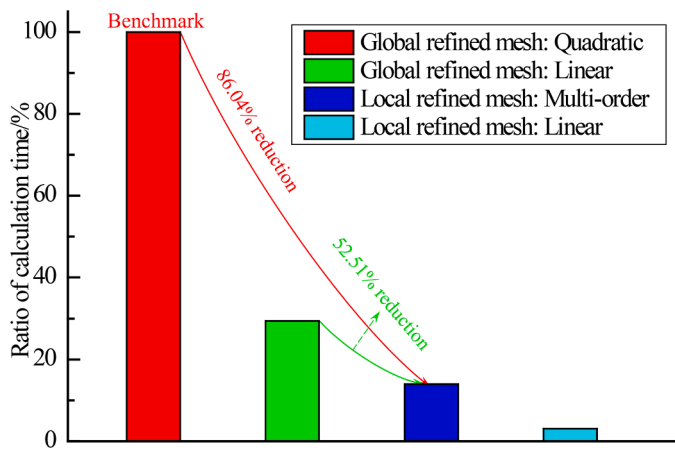


Fig. 26. The comparison of calculation time of different mesh order forms.

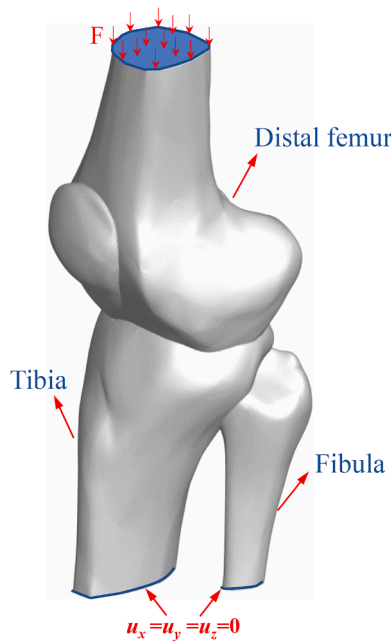


Fig. 27. The 3D model of human knee joint structure.

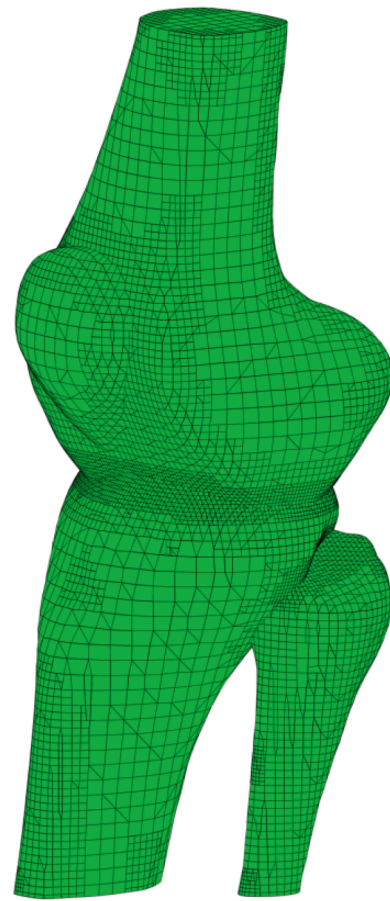


Fig. 28. 3D octree linear mesh of the human knee joint.

The von Mises stress contours for a local refined mesh in the machine screw are illustrated in Fig. 24. As shown in the figure, the stress contours obtained based on linear and multi-order meshes exhibit the same distribution pattern. However, the stress extremes at cross-sections 'A' and 'B', which have been tabulated in Table 5, are different. Notably, the multi-order mesh yields results closer to the benchmarks, and the results remain within an acceptable error range compared to the benchmark. The Dofs of different mesh order forms are shown in Fig. 25, from the figure it can be seen that the local refined multi-order mesh has a significant reduction in Dofs compared to the global refined mesh. Besides, the comparison chart of computational times (Fig. 26) clearly demonstrates that the implementation of a locally refined multi-order mesh significantly enhances computational efficiency.

5. Application of a biomechanical structure

In this section, the static analysis of a structure with human knee joint obtained from CT scans is performed to demonstrate the capability of the proposed method in handling problems with complex geometries.

The size of the knee model is $9.75 \text{ cm} \times 8.23 \text{ cm} \times 23.0 \text{ cm}$ and its geometric shape is shown in Fig. 27, which consists of the tibia, fibula, and distal femur. The material properties of human bones are Young's modulus $E = 12.8 \text{ GPa}$, Poisson's ratio $\nu = 0.3$, and the density $\rho = 1.80 \text{ g/cm}^3$. Accurately modeling the real boundary and loading conditions of the human knee joint is complex, which may be related to the muscle forces and contact forces between the bones. Therefore, the simplified constraints and loading conditions are adopted here, as shown in Fig. 27. All nodes at the bottom of the tibia and fibula are constrained in all degrees of freedom, and the pressure from the upper body is applied uniformly to the femur with a total force of $F = 300 \text{ N}$.

method outlined in Section 2.3.

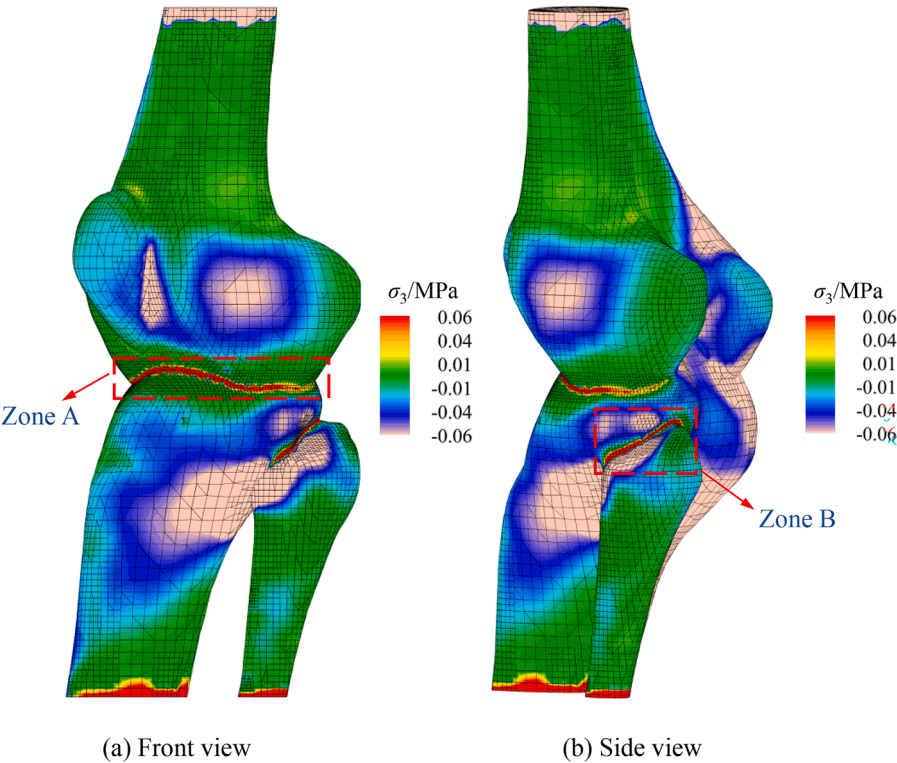


Fig. 29. σ_3 For linear mesh in the human knee joint (Positive represent compressive stress).

Table 6
 σ_3 Extreme values for different meshes.

Mesh form	Stress extreme values/MPa	
	Zone A	Zone B
Linear mesh	4.57	8.98
Multi-order mesh	5.21	9.86

A 3D polyhedron computational mesh based on the octree algorithm is discretized, the maximum and minimum element size in the octree mesh is set as 0.8 cm and 0.1 cm respectively, and the final discretized linear mesh is shown in Fig. 28. From empirical observations, there exists stress concentration phenomenon at different bone contact locations, such as between the femur and tibia, and the tibia and fibula. Therefore, the contact areas between different bones are assigned the minimum element size, as illustrated in Fig. 28. As a result, a total of 43,500 multi-order elements with 53,804 nodes is obtained.

The static analysis is performed in this example, and the distribution contour of the minimum principal stress σ_3 is illustrated in Fig. 29. From the figure, it can be seen that compressive stress tends to concentrate at the junctions of different bones, i.e. regions A and B in Fig. 29, where the stress extreme values are 4.57 MPa and 8.98 MPa, respectively. These two values have been listed in Table 6.

Furthermore, the elements in the joint contact areas are upgraded to quadratic form, as shown in Fig. 30, and the static calculation based on this mesh form is executed. The corresponding distribution contour of σ_3 is depicted in Fig. 31. The distribution pattern of stress concentration remains basically consistent, with the stress extreme values in zones A and B reaching 5.21 MPa and 9.86 MPa, respectively. The comparison of stress values in Table 6 indicate that for the same mesh density, the multi-order mesh proposed in this paper yields more accurate results than the single linear mesh. In scenarios where the mesh density is not particularly high, a multi-order mesh is preferable for enhanced finite element analysis.

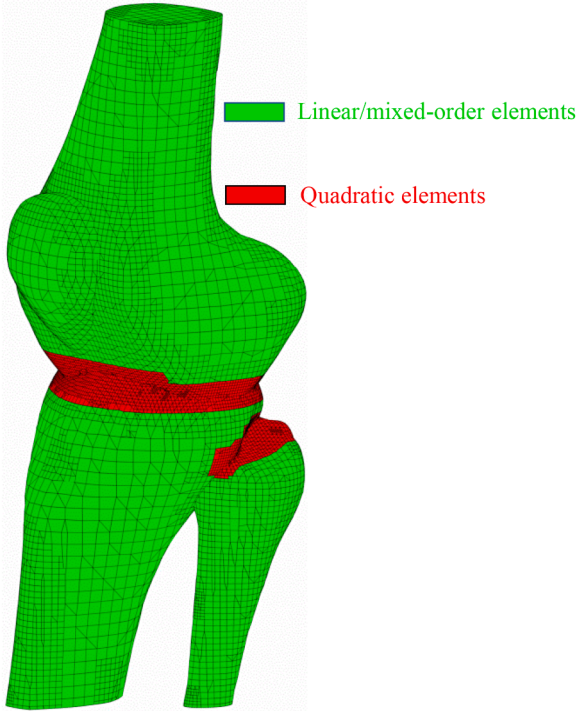


Fig. 30. 3D octree multi-order mesh of the human knee joint.

6. Conclusion

In this paper, based on SBFEM theory, an improved polyhedron element with the mixed-order interpolation functions, which can simultaneously accommodate surfaces with arbitrary order, is proposed to perform 3D high-precision and high-efficiency analysis. Additionally,

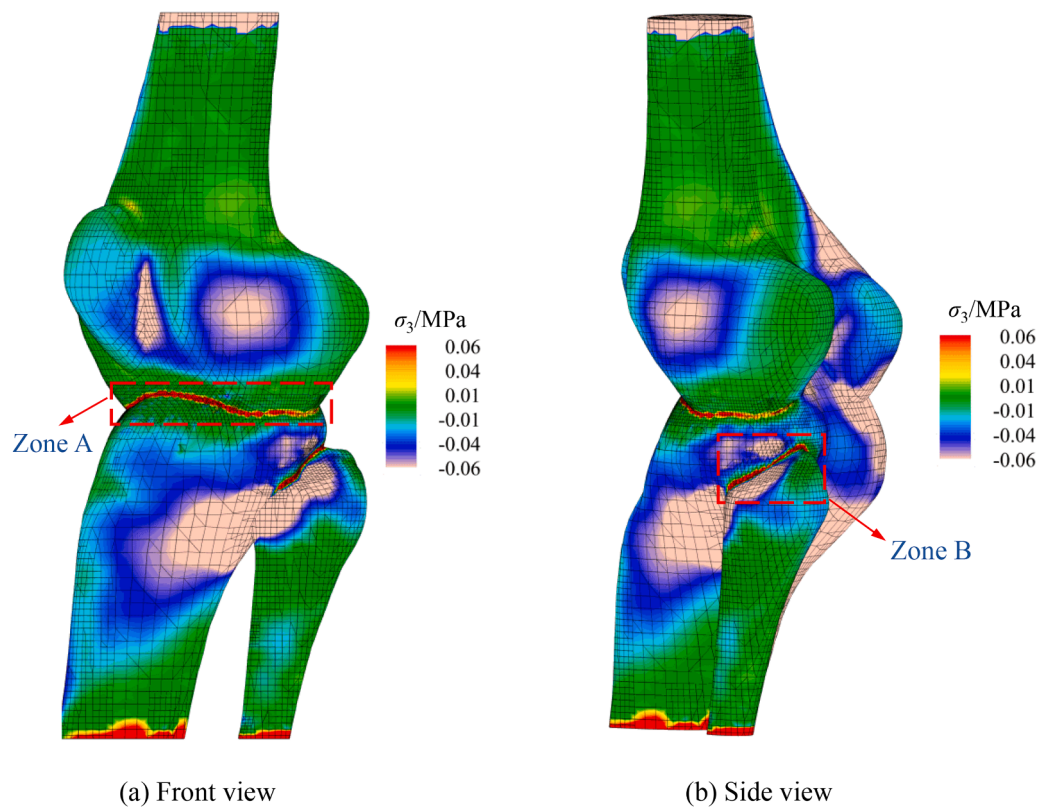


Fig. 31. σ_3 for multi-order mesh in the human knee joint (Positive represent compressive stress).

the polyhedron elements with hanging nodes generated by the octree algorithms are automatically identified and further interpolated in a “mixed-order” form. The accuracy and practicality of the proposed method in modeling bending deformation and stress concentration problems of 3D model are demonstrated through several numerical examples. The main conclusions are as follows:

- (1) The proposed method offers satisfactory computational accuracy and convergence with greatly reduced degrees of freedom. Due to the arbitrary element forms allowed by the proposed method, the available mesh with multi-order forms is able to obtain computational results that deviate by $<3\%$ from the theoretical solutions or the fine numerical solutions, accompanied by a reduction of approximately 35 % in degrees of freedom.
- (2) The proposed method introduces a novel technical means for processing octree meshes. With the help of the employed combinatorial interpolation strategies, surface elements with hanging nodes in polyhedrons can be directly interpolated without the need for additional processing, leading to the enhanced accuracy advantages and practicality, especially in bending-dominated problems.
- (3) The proposed method has good application prospects in certain problems. The allocation scheme for quadratic elements in specific regions, such as local or stress-concentrated regions, results in fine calculation results with a reasonable computational cost. In this manner, the bending deformation and stress concentration problems can be simulated in a more optimal manner.

Finally, the computational efficiency of the proposed method can be further improved by exploring a more optimal integration scheme, which will also be a focus of our future research.

CRediT authorship contribution statement

Xiupeng Nie: Writing – original draft, Software, Methodology, Investigation, Formal analysis. **Degao Zou:** Supervision, Software, Resources, Conceptualization. **Kai Chen:** Writing – review & editing, Visualization, Supervision, Methodology, Conceptualization. **Guoyang Yi:** Software. **Xianjing Kong:** Visualization, Resources, Funding acquisition.

Declaration of competing interest

The authors declare that they have no known competing financial interests or personal relationships that could have appeared to influence the work reported in this paper.

Data availability

Data will be made available on request.

Acknowledgments

This work was supported by the National Natural Science Foundation of China (Grant Nos. 52192674, 52350393, U2240211).

References

- [1] Gao Z, Zhao M, Zhang J, Du X, Wang J. Effect of offset between beam outside and neutral surfaces on dynamic soil-structure interactions. *Soil Dyn Earthq Eng* 2023; 168:107806. <https://doi.org/10.1016/j.soildyn.2023.107806>.
- [2] Gao Z, Zhao M, Du X, Wang J. Effective-mode superposition response spectrum method for three dimensional seismic response analysis of underground structures. *Soil Dyn Earthq Eng* 2023;174:108161. <https://doi.org/10.1016/j.soildyn.2023.108161>.

- [3] Terzini M, Aldieri A, Nurisso S, De Nisco G, Bignardi C. Finite element modeling application in forensic practice: a periprosthetic femoral fracture case study. *Front Bioeng Biotech* 2020;8:619. <https://doi.org/10.3389/fbioe.2020.00619>.
- [4] Jahangir S, Mohammadi A, Mononen M, Hirvasniemi J, Suomalainen J, Saarakkala S, Korhonen R, Tanska P. Rapid X-ray-based 3-D finite element modeling of medial knee joint cartilage biomechanics during walking. *Ann Biomed Eng* 2022;50(6):666–79. <https://doi.org/10.1007/s10439-022-02941-0>.
- [5] Rajanna M, Johnson E, Codoni D, Korobenko A, Bazilevs Y, Liu N, Lua J, Phan N, Hsu M. Finite element methodology for modeling aircraft aerodynamics: development, simulation, and validation. *Comput Mech* 2022;70:549–63. <https://doi.org/10.1007/s00466-022-02178-7>.
- [6] Klotz T, Thabet Y, Walch D. Wing twist angle predictions using finite element model unit load cases. *Res Eng* 2023;18:101088. <https://doi.org/10.1016/j.rineng.2023.101088>.
- [7] Dohrmann C, Heinsteins M, Jung J, Critical S, Witkowski W. Node-based uniform strain elements for three-node triangular and four-node Tetrahedron meshes. *Int J Numer Meth Eng* 2020;47(9):1549–68. [https://doi.org/10.1002/\(SICI\)1097-0207\(20000330\)47:9<1549::AID-NME842>3.0.CO;2-K](https://doi.org/10.1002/(SICI)1097-0207(20000330)47:9<1549::AID-NME842>3.0.CO;2-K).
- [8] Gee M, Dohrmann C, Critical S, Wall W. A uniform nodal strain tetrahedron with isochoric stabilization. *Int J Numer Meth Eng* 2009;78(4):429–43. <https://doi.org/10.1002/nme.2493>.
- [9] Zienkiewicz O, Humpheson C, Lewis R. Associated and non-associated viscoplasticity and plasticity in soil mechanics. *Geotechnique* 1975;25(4):671–89. <https://doi.org/10.1680/geot.1975.25.4.671>.
- [10] Huo S, Liu G, Zhang J, Song C. A smoothed finite element method for octree-based polyhedral meshes with large number of hanging nodes and irregular elements. *Comput Method Appl M* 2020;359:112646. <https://doi.org/10.1016/j.cma.2019.112646>.
- [11] Baldwin K, Schreyer H. Automatic generation of quadrilateral elements by a conformal mapping. *Eng Comput* 1985;2(3):187–94. <https://doi.org/10.1108/eb023618>.
- [12] Yerry M, Shephard M. Automatic three-dimensional mesh generation by the modified-octree technique. *Int J Numer Meth Eng* 1984;20:1965–90. <https://doi.org/10.1002/nme.1620201103>.
- [13] Staten M, Canann S, Owen S. BMSweep: locating interior nodes during sweeping. *Eng Comput* 1999;15:212–8. <https://doi.org/10.1007/s003660050016>.
- [14] Song C, Wolf JP. The scaled boundary finite-element method-alias consistent infinitesimal finite-element cell method-for elastodynamics. *Comput Method Appl M* 1997;147(3-4):329–55. [https://doi.org/10.1016/S0045-7825\(97\)00021-2](https://doi.org/10.1016/S0045-7825(97)00021-2).
- [15] Song C, Wolf JP. The scaled boundary finite-element method: analytical solution in frequency domain. *Comput Methods Appl Mech Eng* 1998;164(1):249–64. [https://doi.org/10.1016/S0045-7825\(98\)00058-9](https://doi.org/10.1016/S0045-7825(98)00058-9).
- [16] Natarajan S, Ooi ET, Saputra A, Song C. A scaled boundary finite element formulation over arbitrary faceted star convex polyhedra. *Eng Anal Bound Elem* 2017;80:218–29. <https://doi.org/10.1016/j.enganabound.2017.03.007>.
- [17] Ooi ET, Saputra A, Natarajan S, Ooi EH, Song C. A dual scaled boundary finite element formulation over arbitrary faceted star convex polyhedra. *Comput Mech* 2020;66:27–47. <https://doi.org/10.1007/s00466-020-01839-9>.
- [18] Song C. Dynamic analysis of unbounded domains by a reduced set of base functions. *Comput Method Appl M* 2006;195(33/36):4075–94. <https://doi.org/10.1016/j.cma.2005.07.011>.
- [19] Song C, Francis T, Gao Wei. Transient dynamic analysis of interface cracks in anisotropic bimaterials by the scaled boundary finite-element method. *Int J Solids Struct* 2010;47:978–89. <https://doi.org/10.1016/j.ijsolstr.2009.12.015>.
- [20] Song C. The scaled boundary finite element method in structural dynamics. *Int J Numer Meth Eng* 2009;77(8):1139–71. <https://doi.org/10.1002/nme.2454>.
- [21] Zhang P, Du C, Birk C, Zhao W. A scaled boundary finite element method for modelling wing crack propagation problems. *Eng Fract Mech* 2019;216:106466. <https://doi.org/10.1016/j.engfractmech.2019.04.040>.
- [22] Zhang P, Du C, Zhao W, Sun L. Dynamic crack face contact and propagation simulation based on the scaled boundary finite element method. *Comput Method Appl M* 2021;385:114044. <https://doi.org/10.1016/j.cma.2021.114044>.
- [23] Du C, Huang W, Ghaemian M, Jiang S, Zhao Z. New nonlocal multiscale damage model for modelling damage and cracking in quasi-brittle materials. *Eng Fract Mech* 2023;277:108927. <https://doi.org/10.1016/j.engfractmech.2022.108927>.
- [24] Song C, Ooi E, Pramod A, Natarajan S. A novel error indicator and an adaptive refinement technique using the scaled boundary finite element method. *Eng Anal Bound Elem* 2018;94:10–24. <https://doi.org/10.1016/j.enganabound.2018.05.010>.
- [25] Natarajan S, Ooi E, Birk C, Song C. Adaptive modelling of dynamic brittle fracture-a combined phase field regularized cohesive zone model and scaled boundary finite element approach. *Int J Fracture* 2022;236(1):87–108. <https://doi.org/10.1007/s10704-022-00634-2>.
- [26] Liu L, Zhang J, Song C, Birk C, Gao W. An automatic approach for the acoustic analysis of three-dimensional bounded and unbounded domains by scaled boundary finite element method. *Int J Mech Sci* 2019;151:563–81. <https://doi.org/10.1016/j.ijmecsci.2018.12.018>.
- [27] Liu L, Zhang J, Song C, Birk C, Saputra AA, Gao W. Automatic three-dimensional acoustic-structure interaction analysis using the scaled boundary finite element method. *J Comput Phys* 2019;395:432–60. <https://doi.org/10.1016/j.jcp.2019.06.033>.
- [28] Zhang J, Ankita A, Gravenkamp H, Eisenträger S, Song C. A massively parallel explicit solver for elasto-dynamic problems exploiting octree meshes. *Comput Method Appl Mech Eng* 2021;380:113811. <https://doi.org/10.1016/j.cma.2021.113811>.
- [29] Zhang J, Zhao M, Eisenträger S, Du X, Song C. An asynchronous parallel explicit solver based on scaled boundary finite element method using octree meshes. *Comput Method Appl Mech Eng* 2022;401:115653. <https://doi.org/10.1016/j.cma.2022.115653>.
- [30] Zhang G, Zhao M, Du X, Zhang J. Time-domain scaled boundary perfectly matched layer for elastic wave propagation. *Int J Numer Meth Eng* 2023;124:3906–34. <https://doi.org/10.1002/nme.7300>.
- [31] Zhang G, Zhao M, Zhang J, Du X. Scaled Boundary Perfectly Matched Layer (SBPML): a novel 3D time-domain artificial boundary method for wave problem in general-shaped and heterogeneous infinite domain. *Comput Method Appl Mech Eng* 2023;403:115738. <https://doi.org/10.1016/j.cma.2022.115738>.
- [32] Zhang G, Zhao M, Zhang J, Wang J, Du X. Scaled boundary perfectly matched layer for wave propagation in a three-dimensional poroelastic medium. *Appl Math Model* 2024;125:108–38. <https://doi.org/10.1016/j.apm.2023.09.028>.
- [33] Zhang G, Zhao M, Zhang Du X. Prismatic-element SBPML coupled with SBFEM for 3D infinite transient wave problems. *Comput Method Appl Mech Eng* 2024;427(2024):117014. <https://doi.org/10.1016/j.cma.2024.117014>.
- [34] Zhang J, Zhao M, Zhang G, Zhang J, Du X. 3D acoustic scaled boundary perfectly matched layer (SBPML) for acoustic-structure interaction problems. *Eng Anal Bound Elem* 2024;164:105765. <https://doi.org/10.1016/j.enganabound.2024.105765>.
- [35] Ye W, Liu J, Zhang J, Yang F, Lin G. A new semi-analytical solution of bending, buckling and free vibration of functionally graded plates using scaled boundary finite element method. *Thin Wall Struct* 2021;163:107776. <https://doi.org/10.1016/j.tws.2021.107776>.
- [36] Ye W, Liu J, Zang Q, Yin Z, Lin G. Buckling analysis of three-dimensional functionally graded sandwich plates using two-dimensional scaled boundary finite element method. *Mech Adv Mater Struct* 2022;29(17):2468–83. <https://doi.org/10.1080/15376494.2020.1866125>.
- [37] Zou D, Chen K, Kong X, Liu J. An enhanced octree polyhedral scaled boundary finite element method and its applications in structure analysis. *Eng Anal Bound Elem* 2017;84:87–107. <https://doi.org/10.1016/j.enganabound.2017.07.007>.
- [38] Chen K, Zou D, Kong X, Yu X. An efficient nonlinear octree SBFEM and its application to complicated geotechnical structures. *Comput Geotech* 2018;96:226–45. <https://doi.org/10.1016/j.compgeo.2017.10.021>.
- [39] Chen K, Zou D, Kong X, Zhou Y. Global concurrent cross-scale nonlinear analysis approach of complex CFRD systems considering dynamic impervious panel-rockfill material-foundation interactions. *Soil Dyn Earthq Eng* 2018;114:51–68. <https://doi.org/10.1016/j.soildyn.2018.06.027>.
- [40] Chen K, Zou D, Kong X, Liu J. Elasto-plastic fine-scale damage failure analysis of metro structures based on coupled SBFEM-FEM. *Comput Geotech* 2019;108:280–94. <https://doi.org/10.1016/j.compgeo.2018.12.030>.
- [41] Nie X, Zou D, Chen K, Liu J, Kong X, Qu Y. The versatile polyhedral elements of Cosserat continuum theory based on SBFEM and its application. *Eng Anal Bound Elem* 2024;162:87–101. <https://doi.org/10.1016/j.enganabound.2024.02.001>.
- [42] Su R, Tangaramvong S, Song C. Automatic image-based SBFE-BESO approach for topology structural optimization. *Int J Mech Sci* 2024;263:108773. <https://doi.org/10.1016/j.ijmecsci.2023.108773>.
- [43] Zhang J, Eisenträger S, Zhan Y, Saputra A, Song C. Direct point-cloud-based numerical analysis using octree meshes. *Comput Struct* 2023;289:107175. <https://doi.org/10.1016/j.compstruc.2023.107175>.
- [44] Talebi H, Saputra A, Song C. Stress analysis of 3D complex geometries using the scaled boundary polyhedral finite elements. *Comput Mech* 2016;58:697–715. <https://doi.org/10.1007/s00466-016-1312-0>.
- [45] Taylor R, Beresford P, Wilson E. A non-conforming element for stress analysis. *Int J Numer Meth Eng* 1976;10(6):1211–9. <https://doi.org/10.1002/nme.1620100602>.
- [46] Barrett K. Multilinear Jacobians for iso-parametric planar elements. *Finite Elem Anal Des* 2004;40(8):821–53. [https://doi.org/10.1016/S0168-874X\(03\)00116-1](https://doi.org/10.1016/S0168-874X(03)00116-1).
- [47] Zalmal M. A remark on the 'serendipity family'. *Int J Num Meth Eng* 1973;7(1):98–100. <https://doi.org/10.1002/nme.1620070109>.
- [48] Lee C, Hobbs R. On using different finite elements with an automatic adaptive refinement procedure for the solution of 2-D stress analysis problems. *Int J Numer Meth Eng* 1997;40(24):4547–76. [https://doi.org/10.1002/\(SICI\)1097-0207\(19971230\)40:24<4547::AID-NME272>3.0.CO;2-J](https://doi.org/10.1002/(SICI)1097-0207(19971230)40:24<4547::AID-NME272>3.0.CO;2-J).
- [49] Hormann K, Floater M. Mean value coordinates for arbitrary planar polygons. *ACM T Graphic* 2006;25(4):1424–41. <https://doi.org/10.1145/1183287.1183295>.
- [50] Floater MS, Lai MJ. Polygonal spline spaces and the numerical solution of the Poisson equation. *SIAM J Numer Anal* 2016;54(2):797–824. <https://doi.org/10.1137/15M101155X>.
- [51] Grbić S, Jelenić G, Ribarić D. Quadrilateral 2D linked-interpolation finite elements for micropolar continuum. *Acta Mech Sinica-Prc* 2019;35:1001–20. <https://doi.org/10.1007/s10409-019-00870-1>.
- [52] Cao J, Xiao Y, Xiao Y, Chen Z, Xue F, Wei X, Zhang Y. Quadratic serendipity element shape functions on general planar polygons. *Comput Method Appl M* 2022;392:114703. <https://doi.org/10.1016/j.cma.2022.114703>.
- [53] Chen K, Zou D, Liu J, Zhuo Y. A high-precision formula for mixed-order polygon elements based on SBFEM. *Comput Geotech* 2023;155:105209. <https://doi.org/10.1016/j.compgeo.2022.105209>.
- [54] Nie X, Zou D, Chen K, Kong X, Yi G. A SBFEM formula for the mixed-order hexahedron interpolation based on serendipity elements. *Eng Anal Bound Elem* 2024;164:105760. <https://doi.org/10.1016/j.enganabound.2024.105760>.

- [55] Deeks A, Wolf J. A virtual work derivation of the scaled boundary finite-element method for elastostatics. *Comput Mech* 2002;28:489–504. <https://doi.org/10.1007/s00466-002-0314-2>.
- [56] Zou D, Kong X, Liu J, et al. Theoretical introduction and user manual of the GEODYNA7.0: a high-performance finite element analysis software system for large-scale geotechnical engineering. Institute of earthquake engineering, Dalian University of Technology: Dalian; 2022.
- [57] Timoshenko S, Goodier J. *Theory of elasticity*. New York: McGrawHill; 1970.